Supplementary materials to:
RF-free driving of nuclear spins with color centers in silicon carbide

Raphael Wörnle,[1,2,3,*] Jonathan Körber,[1,2] Timo Steidl,[1,2] Georgy V. Astakhov,[4]
Durga B. R. Dasari,[1,2] Florian Kaiser,[5,6] Vadim Vorobyov,[1,2] and Jörg Wrachtrup[1,2,3]

[1] *3rd Institute of Physics, University of Stuttgart, Allmandring 13, 70569 Stuttgart, Germany.*
[2] *Center for Integrated Quantum Science and Technology, 70569 Stuttgart, Germany.*
[3] *Max Planck Institute for Solid State Research, Heisenbergstraße 1, 70569 Stuttgart, Germany.*
[4] *Helmholtz-Zentrum Dresden-Rossendorf, Institute of Ion Beam Physics and Materials Research, 01328 Dresden, Germany.*
[5] *Quantum Materials, Luxembourg Institute of Science and Technology (LIST),*
28 Avenue des Hauts Fourneaux, 4362 Belval, Luxembourg.
[6] *University of Luxembourg, 2 Avenue de l'Université, 4365 Belval, Luxembourg.*

(Dated: January 29, 2026)

S1. SINGLE DEFECT VERIFICATION

For the defects investigated in the main part, autocorrelation measurements were performed in the so-called Hanbury-Brown & Twiss interferometry experiment. The background-corrected measurements are shown for the PL6 center in Figure S1a and for the PL6 center with coupled nuclear spin in Figure S1b. Assuming a three level system for our defect [1], the theoretical second-order correlation measurement can be fitted using

$$g^{(2)}(\tau) = \frac{1}{N}\left(1 - (1-a)\cdot \mathrm{e}^{-\frac{\tau}{\tau_1}} + a\cdot \mathrm{e}^{-\frac{\tau}{\tau_2}}\right) + \frac{N-1}{N} \quad \text{with} \quad g^{(2)}(\tau) \overset{\tau\to 0}{=} 1 - \frac{1}{N}, \tag{1}$$

where a, τ_1 and τ_2 are the amplitude and the (anti-)bunching time constants and N the number of emitters [2]. The results in both cases yield values of $g^{(2)}(0) \ll 0.5$, which clearly confirms that each emitter is a single emitter.

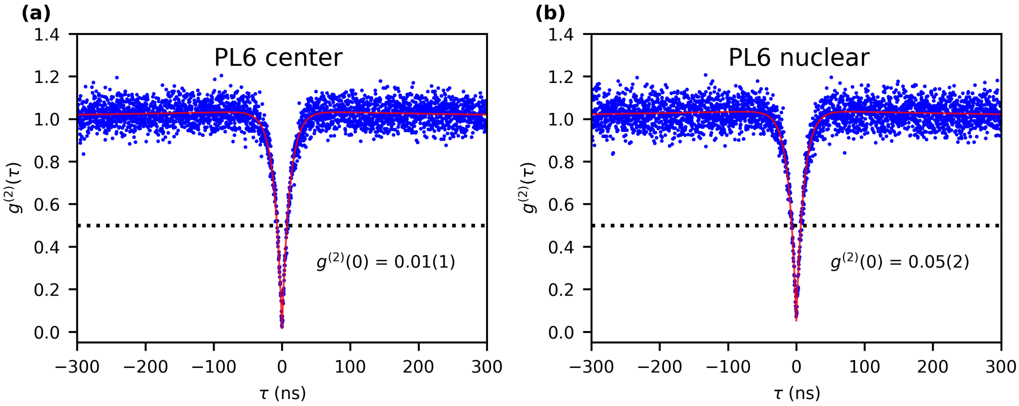

Figure S1: Autocorrelation measurements of PL6 centers. Background-corrected autocorrelation measurements measured at an excitation laser power of 100 µW for **(a)** a single PL6 center and **(b)** for the PL6 center coupled with a nearby nuclear spin. The fitted values for zero time delay yields a value of $g^{(2)}(0) = 0.01(1)$ for the PL6 center and $g^{(2)}(0) = 0.05(2)$ for the nuclear spin coupled PL6 center, both confirming the nature as single defects.

---

[*] E-Mail: raphael.woernle@pi3.uni-stuttgart.de

S2. NUCLEAR SPIN CONTROL

A. Nuclear spin identification

The nuclear spin defect shown in Figure 2b in the main text can also be experimentally classified to determine which type of nuclear spin it is. Hahn echo measurements are used for this purpose in a magnetic field of 145 G experimentally, which is illustrated in Figure S2. The relationship between the Larmor frequencies $f_\mathrm{L} \propto \gamma_\mathrm{N} \cdot B$ results in a gyromagnetic ratio of $\gamma_\mathrm{N} = 10.88 \pm 0.12$ from the measurement, which corresponds relatively closely to the gyromagnetic ratio of $\gamma_\mathrm{N}^{^{13}\mathrm{C}} = 10.71$, therefore confirming the presence of a ^{13}C nuclear spin.

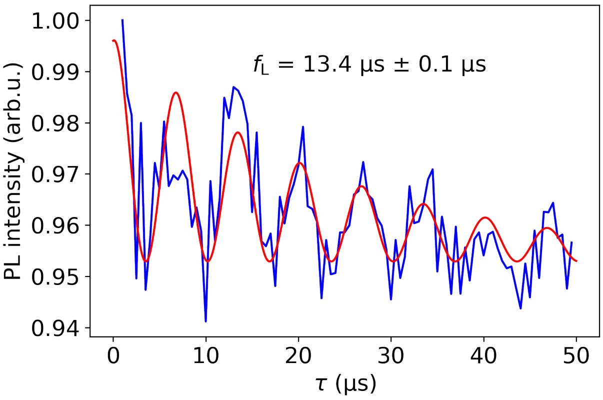

Figure S2: Nuclear spin identification. Hahn echo measurement on the PL6 with coupled nuclear spin in an external magnetic field of 145 G yielding a gyromagnetic ratio of $\gamma_\mathrm{N} = 10.88 \pm 0.12$ matching the one for a ^{13}C nuclear spin.

This sequence can now be modified, resulting in the Hahn echo measurements of the nuclear spin in the main part in Figure 4.

B. Coupling strength

Exact control over the nuclear spin can only be achieved if the phase between the two nuclear spin states can also be manipulated. The exact strength of the coupling of the nuclear spin shown in Figure 2b in the main text can be determined using the following pulse sequence, shown in figure S3a. The idea and implementation were taken from [3]. For this purpose, the nuclear spin is initialized similarly as for the precession measurements.

Furthermore, a strong, non-selective π pulse excites both nuclear spin states; the subsequent waiting period before the second π pulse creates a relative phase on the nuclear spin state. Subsequently, a weak π pulse on the electron spin maps the system back onto the electron spin for read out, and the oscillations at the hyperfine coupling frequency ω_1 can be observed. In this case, a coupling strength of $\omega_1 = 2\pi \cdot 6.69(5)$ MHz is determined and shown in Figure S3b.

This sequence can now be modified, resulting in the Hahn echo measurements of the nuclear spin in the main part in Figure 4.

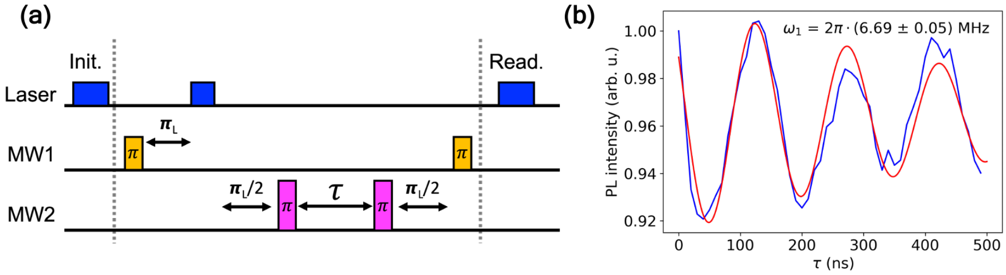

Figure S3: Nuclear spin coupling. (a) Measurement sequence for determining the exact coupling strength of the coupled nuclear spin. Sequence adapted from [3]. **(b)** Experimental result including damped cosine fit yielding a coupling strength of $\omega_1 = 2\pi \cdot 6.69(5)$ MHz.

C. Polarization

The sequence with the polarization step shown in Figure 2c in the main part can be extended by repeating the polarization step N times. The resonant driving of the nuclear spin polarizes it, thus improving the contrast. This is illustrated in Figure S4a in dependence of the number of polarization steps. It shows a saturation behavior whereby the contrast reaches almost twice the contrast of the CW-ODMR measurement seen in the main part in Figure 2b.

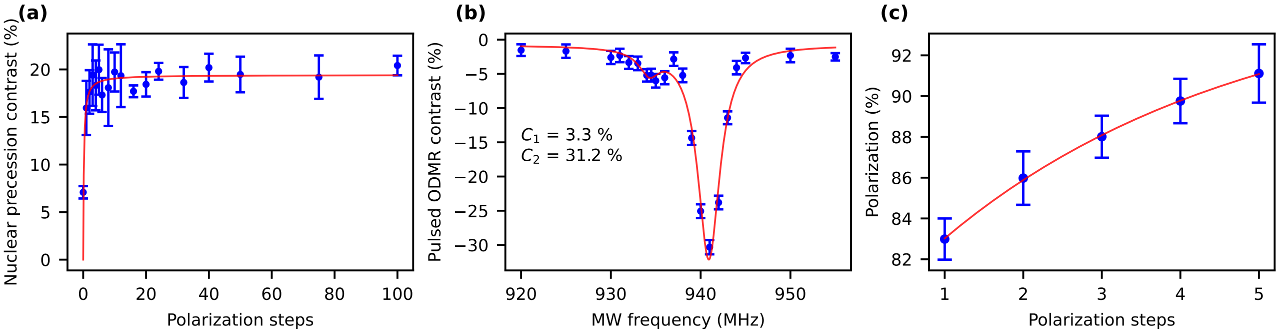

Figure S4: Polarization saturation study. (a) Saturation study of the measured contrast of the nuclear precession in dependence of the number of polarization steps with saturation fit $C = {}^{(C_{\text{Sat}}\cdot N)}/_{(N+N_{\text{Sat}})}$ yielding a saturation contrast of 19.4 ± 0.7 %. Error bars are determined by the fitted contrast and fit error of each measurement. **(b)** Pulsed ODMR measurement after previous polarization of nuclear spin yielding to a almost vanishing transition of the $|-1,\uparrow\rangle$ transition whereas the $|-1,\downarrow\rangle$ transition contrast is maximal. **(c)** Polarization study of ratios of the pulsed ODMR contrasts in dependence of the number of polarization steps with corresponding fit function yielding a saturation polarization behavior of 95.5 ± 0.8 %.

Additionally, high polarization can be achieved through repeating the shown polarization step in figure 2d in the main part multiple times, which has been shown to result in almost complete transition suppression. This is clearly achieved by performing $N = 5$ polarization steps and measuring pulsed ODMR. The result can be seen in Figure S4b, where a high degree of polarization is shown. In addition, a polarization study can be performed to determine the dependence of the polarization steps, as shown in Figure S4c. For this purpose, the polarization was determined from the ratio of the contrast of the two ODMR transitions. This results in a polarization of 95 % between the two states (in this case, $|-1,\uparrow\rangle$ and $|-1,\downarrow\rangle$). From this ratio, the effective zero-spin temperature can be determined using

$$p_\uparrow = p_\downarrow \cdot \exp\left(\frac{-\gamma_0 B}{k_B T}\right) \tag{2}$$

with $\omega_0 = \gamma_0 B$ as the Larmor precession frequency. In our case, the effective nuclear spin temperature gets calculated to $T_{\text{nucl}} = 400$ nK. The idea was first shown by Dutt et al. (Suppl. S.2.4.2) [4].

S3. SECOND-ORDER PERTURBATION DERIVATION

In this section we derive the effective Hamiltonian acting on the nuclear spin within the $m_s = 0$ manifold of an $S = 1$ electronic spin coupled to a nuclear spin $I = 1/2$. The derivation follows the Van Vleck (Schrieffer–Wolff) perturbation procedure to second order, with all intermediate steps shown.

1. Full Hamiltonian and Hilbert-Space Partition

The complete spin Hamiltonian is

$$H = DS_z^2 + E(S_x^2 - S_y^2) + \gamma_e \mathbf{B} \cdot \mathbf{S} + \mathbf{S} \cdot \mathbf{A} \cdot \mathbf{I} - \gamma_I \mathbf{B} \cdot \mathbf{I}, \tag{3}$$

where $D \gg \gamma_e B, A_\perp$. We project the dynamics onto the two-dimensional subspace

$$\mathcal{H}_0 = \{|0,\uparrow\rangle, |0,\downarrow\rangle\},$$

while the electronic levels $|m_s = \pm 1\rangle$ form the excited subspace $\mathcal{H}_1$.

We decompose:

$$H = H_0 + V, \tag{4}$$

where the unperturbed part is

$$H_0 = DS_z^2 + \gamma_e B_z S_z, \tag{5}$$

and the perturbation

$$V = \gamma_e (B_x S_x + B_y S_y) + \mathbf{S} \cdot \mathbf{A} \cdot \mathbf{I} - \gamma_I \mathbf{B} \cdot \mathbf{I}. \tag{6}$$

The unperturbed energies are

$$E_0 = 0, \tag{7}$$
$$E_+ = D + \gamma_e B_z, \tag{8}$$
$$E_- = D - \gamma_e B_z. \tag{9}$$

2. Matrix Elements of S_x and S_y

For an $S = 1$ spin:

$$\langle 0|S_x| \pm 1\rangle = \frac{1}{\sqrt{2}}, \tag{10}$$
$$\langle 0|S_y| \pm 1\rangle = \pm\frac{i}{\sqrt{2}}. \tag{11}$$

Define

$$B_\pm = B_x \pm iB_y.$$

Then

$$Z_\pm \equiv \langle 0|\gamma_e (B_x S_x + B_y S_y)| \pm 1\rangle = \frac{\gamma_e}{\sqrt{2}} B_\pm. \tag{12}$$

3. Off-Axis Hyperfine Terms

$$\mathbf{S}\cdot\mathbf{A}\cdot\mathbf{I} = A_{\|} S_z I_z + A_{\perp}(S_x I_x + S_y I_y).$$

Since $S_z|0\rangle = 0$, the term with $A_{\|}$ vanishes in this subspace. Thus

$$V_{\mathrm{hf},\perp} = A_{\perp}(S_x I_x + S_y I_y) = \frac{A_{\perp}}{2}(S_+ I_- + S_- I_+).$$

Using $\langle 0|S_{\pm}|\pm 1\rangle = 1/\sqrt{2}$:

$$H_+ = \langle 0|V_{\mathrm{hf},\perp}|+1\rangle = \frac{A_{\perp}}{\sqrt{2}} I_-, \tag{13}$$

$$H_- = \langle 0|V_{\mathrm{hf},\perp}|-1\rangle = \frac{A_{\perp}}{\sqrt{2}} I_+. \tag{14}$$

4. Van Vleck / Schrieffer–Wolff Formula

Projector P acts on $\mathcal{H}_0$. The effective Hamiltonian up to second order is:

$$H_{\mathrm{eff}} = PVP - \sum_{m=\pm 1} PV|m\rangle \frac{1}{E_m - E_0}\langle m|VP. \tag{15}$$

The first-order term gives the nuclear Zeeman interaction. The second-order sum contains the hyperfine-enhanced corrections.

5. Diagonal Second-Order Correction (ν_z)

Use:

$$H_{\pm}H_{\pm}^{\dagger} = \frac{A_{\perp}^2}{2}(I_x^2 + I_y^2) = \frac{A_{\perp}^2}{2}\cdot\frac{1}{4},$$

because $I = 1/2$.
Thus:

$$\nu_z = \frac{A_{\perp}^2}{2}\left(\frac{1}{E_+} + \frac{1}{E_-}\right) = A_{\perp}^2 \frac{E_+ + E_-}{2E_+E_-}. \tag{16}$$

Using:

$$E_+ + E_- = 2D, \quad E_+E_- = D^2 - (\gamma_e B_z)^2,$$

we obtain:

$$\boxed{\nu_z = \frac{\gamma_e B_z A_{\perp}^2}{D^2 - (\gamma_e B_z)^2}.} \tag{17}$$

6. Off-Diagonal Second-Order Term ($\nu_{\perp}$)

Mixed Zeeman–hyperfine processes produce:

$$H_{\mathrm{eff}}^{(2)} \supset -\sum_{m=\pm 1}\frac{1}{E_m}(Z_m H_m^{\dagger} + H_m Z_m^{\dagger}). \tag{18}$$

1. Contribution from m = +1:

$$Z_+ H_+^\dagger = \frac{\gamma_e A_\perp}{2} B_+ I_+, \qquad H_+ Z_+^\dagger = \frac{\gamma_e A_\perp}{2} B_- I_-.$$

2. Contribution from m = -1:

$$Z_- H_-^\dagger = \frac{\gamma_e A_\perp}{2} B_- I_-, \qquad H_- Z_-^\dagger = \frac{\gamma_e A_\perp}{2} B_+ I_+.$$

Summing both:

$$\frac{\gamma_e A_\perp}{2} (B_+ I_+ + B_- I_-) \left(\frac{1}{E_+} + \frac{1}{E_-} \right). \tag{19}$$

Use identity:

$$B_+ I_+ + B_- I_- = 2(B_x I_x + B_y I_y) = 2B_\perp I_x \quad \text{(choosing } \parallel B_\perp\text{)}.$$

Thus:

$$\nu_\perp = -\frac{2\gamma_e B_\perp A_\perp D}{D^2 - (\gamma_e B_z)^2}. \tag{20}$$

7. Final Effective Hamiltonian

Putting all the terms together:

$$\boxed{H_{\text{eff}} = \frac{1}{2} \begin{pmatrix} \gamma_I B_z + \nu_z & \gamma_I B_\perp + \nu_\perp \\ \gamma_I B_\perp + \nu_\perp & -(\gamma_I B_z + \nu_z) \end{pmatrix}.} \tag{21}$$

This is the effective nuclear-spin Hamiltonian used in the main text. It contains both hyperfine-enhanced longitudinal energy shifts and hyperfine-mediated transverse couplings arising from virtual electronic excitations.

S4. MAGNETIC FIELD OPTIMIZATION

In addition to the method described in the main part for aligning the magnet using nuclear spin precessions, there are three other methods, which are described below.

A. Optimization via count rate

The simplest and fastest method of aligning the magnetic field is by optimizing the count rate of a single PL6 center. For PL6 centers, the detected count rate is maximum when the magnetic field is aligned due to the inter system crossing rates of the Spin 1 system. The misalignment results in spin mixing, which partially pumps the system to the $m_s = 1$ or $m_s = -1$ state, causing the count rate to decrease. For the measurements, the lateral position of the magnet is swept and the count rate is measured for a fixed magnetic field. This is shown in Figure S5a for an applied external magnetic field. By fitting a 2D Gaussian function, the maximum count rate and thus the position with the best alignment can be found.

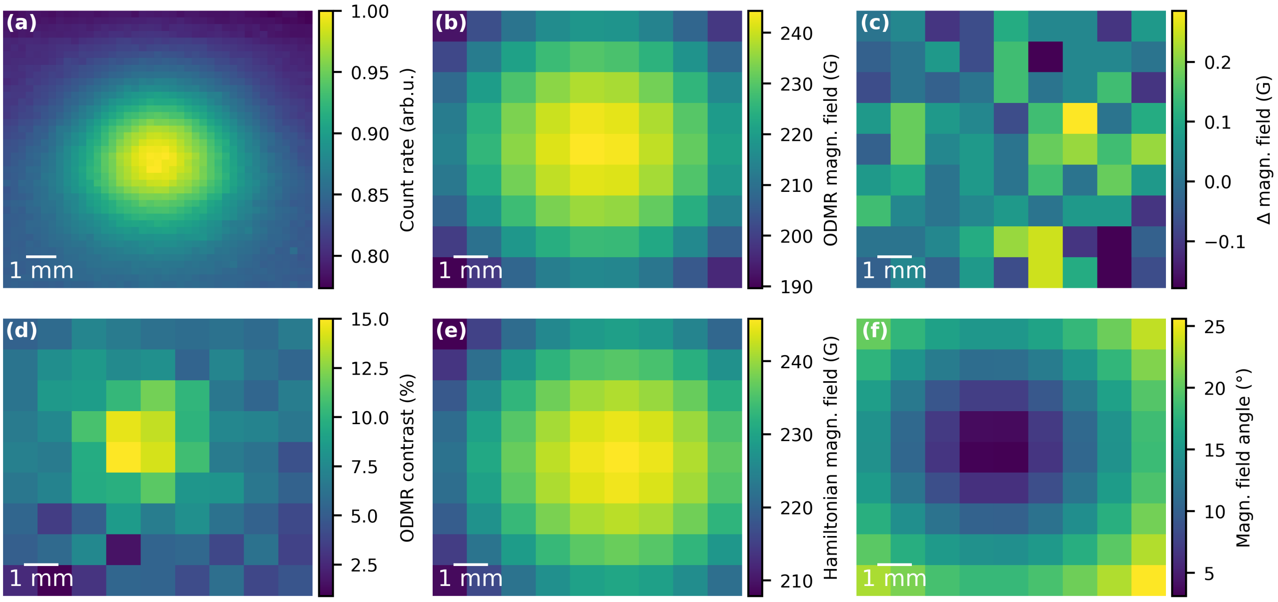

Figure S5: Magnetic field optimization. All measurements were done by sweeping the lateral position of the magnet in a fixed height above the sample. **(a)** Count rate of a single PL6 center in dependence of the external magnetic field. **(b)** Measured magnetic field via the $|-1\rangle$ and $|+1\rangle$ ODMR transitions. **(c)** Reproducibility study of the measurement in **(b)** by remeasuring the magnetic field and determining the differences compared to the first measurement to show a repetition and exact alignment of the magnet is given. **(d)** Contrast of the $|+1\rangle$ transition in dependence of the magnetic field position. **(e) & (f)** Calculated external magnetic field strength and angle via the Hamiltonian.

B. Optimization via ODMR measurements

Another way to determine alignment is with ODMR measurements. When the magnetic field is aligned, the ODMR splitting between the two transitions is maximal, while it is reduced for deviations in alignment.

As with the count rate measurements, the lateral position of the magnet is swept, and for a single PL6 center, the ODMR transition $m_s = 0 \rightarrow m_s = \pm 1$ is measured and fitted with a 2D Gaussian function to find the ideal magnet position. From the difference between the two ODMR frequencies one can calculate the magnetic field strength which is depicted in Figure S5b. Furthermore, it is important to determine whether a reproducible magnet position can be achieved to enable precise alignment. A repetition of the experiment in Figure S5b and subsequent comparison are shown in Figure S5c. It shows that only minimal differences in the magnetic field arise, which can be explained by the fitting uncertainty of the ODMR measurements. In addition, a clear dependence of the contrast in the ODMR measurement can be seen, which is shown in Figure S5d.

C. Optimization via Hamiltonian

With the ODMR frequencies already determined, the alignment can also be done using the Hamiltonian. This was already shown by Balasubramanian et al. in 2008 [5]. Here, only an abbreviated derivation is discussed.

In summary, from the reduced Hamiltonian to the electron spin from equation 1 in the main part, the magnetic field is characterized by the absolute strength B and the two polar and azimuthal angles Θ and φ by transforming the coordinates into polar coordinates. The position of the spin levels can be determined by solving the following equation for x

$$x^3 - \left(\frac{D^2}{3} + E^2 + \beta^2\right)x - \frac{\beta^2}{2}\left(D\cos(2\Theta) + 2E\cos(2\phi)\sin^2(\Theta)\right) - \frac{D}{6}\left(4E^2 + \beta^2\right) + \frac{2D^3}{27} = 0 \tag{22}$$

with $\beta = \mu_\mathrm{B} g B$. The relation

$$\Delta = D\cos(2\Theta) + 2E\cos(2\varphi)\sin^2(\Theta) \tag{23}$$

leads to

$$\beta^2 = \frac{1}{3}\left(\nu_1^2 + \nu_2^2 - \nu_1\nu_2 - D^2\right) - E^2 \tag{24}$$

and

$$\Delta = \frac{7D^3 + 2(\nu_1 + \nu_2)(2(\nu_1^2 + \nu_2^2) - 5\nu_1\nu_2 - 9E^2) - 3D(\nu_1^2 + \nu_2^2 - \nu_1\nu_2 + 9E^2)}{9(\nu_1^2 + \nu_2^2 - \nu_1\nu_2 - D^2 - 3E^2)} \xrightarrow{D \gg E} \Delta \approx D\cos(2\theta) \tag{25}$$

for solutions for the magnetic field strength and the tilt angle and are illustrated in figure S5e & S5f.

S5. TOMOGRAPHY

A more detailed description of the tomographies of electron spin, nuclear spin and the coupled two-qubit system shown in Figure 5 in the main part follows here.

A. Electron spin

For the simple one-qubit case, electron spin tomography can be determined using Rabi oscillations. The system is initialized to the $m_s = 0$ state, in this case the transition $m_s = 0 \rightarrow m_s = -1$ is driven by a resonant microwave pulse, and finally, before the readout, one of three possible pulses is taken to measure the individual bases. No additional pulse is taken for the Z basis; for X and Y, a $\pi/2$ pulse is applied in the X- or Y-direction. This is achieved using the 90 ° phase shifter. The corresponding pulse sequence is shown schematically in Figure S6a.

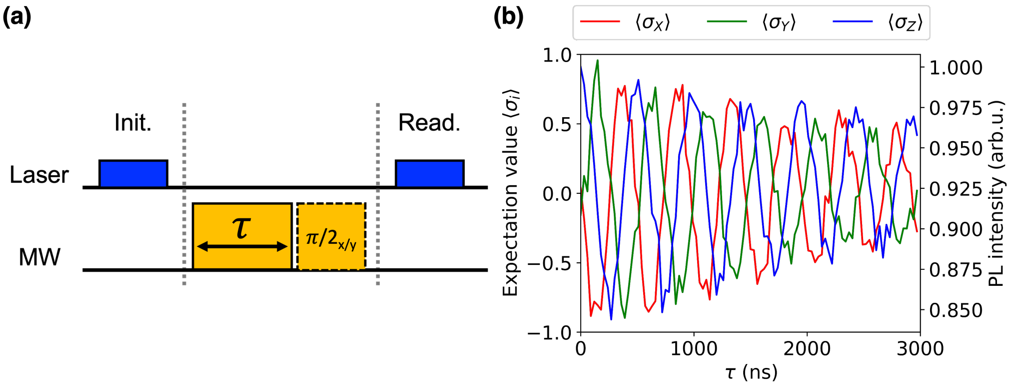

Figure S6: Electron spin tomography. (a) Measurement sequence for the electron spin tomography. For the Z basis, no additional pulse is applied whereas for the X and Y basis, a $\pi/2$ pulse in the corresponding direction is applied. **(b)** Experimental result for the electron spin tomography. The determined expectation values can be seen in Table S1.

Experimentally, the following three expectation values for X, Y, and Z are obtained, which are shown in Table S1. The absolute measured Rabi contrast is normalized to obtain an expectation value between -1 and 1. This is shown in Figure S6b. The first data point was used for the tomography because, as can be seen experimentally, the Rabi oscillations show exponential decay, and thus a false result would otherwise be formed.

Table S1: Electron spin tomography. Experimentally determined expectation values for the electron spin.

S_i	$\langle S_i\rangle$
Z	0.9353
X	0.0394
Y	-0.1555

Using these three expectation values, the density matrix for a one-qubit system can be determined. This works as follows:

$$\rho = \frac{1}{2}\left(I + \sum_i \langle S_i\rangle \sigma_i\right) \tag{26}$$

where I is the identity matrix and σ_i are the Pauli matrices.

$$I = \begin{pmatrix} 1 & 0 \\ 0 & 1 \end{pmatrix}, \quad X = \begin{pmatrix} 0 & 1 \\ 1 & 0 \end{pmatrix}, \quad Y = \begin{pmatrix} 0 & -i \\ i & 0 \end{pmatrix}, \quad Z = \begin{pmatrix} 1 & 0 \\ 0 & -1 \end{pmatrix} \tag{27}$$

Using the experimental parameters, the density matrix can be reconstructed, and to determine the fidelity, the experimentally determined state is compared to the ideal state $|\Psi^+\rangle$ with

$$|\Psi^+\rangle = \begin{pmatrix} 1 & 0 \\ 0 & 0 \end{pmatrix} \tag{28}$$

and the fidelity F is determined as follows

$$F = \mathrm{Tr}\left(\sqrt{\sqrt{\rho}\rho'\sqrt{\rho}}\right) \tag{29}$$

where ρ is the experimentally determined density matrix and ρ' the Bell state matrix.

B. Nuclear spin

For nuclear spin, tomography works in theory in exactly the same way as for electron spin. However, the nuclear spin cannot be read directly; therefore, as in all measurements, it is projected onto the electron spin to be read out.

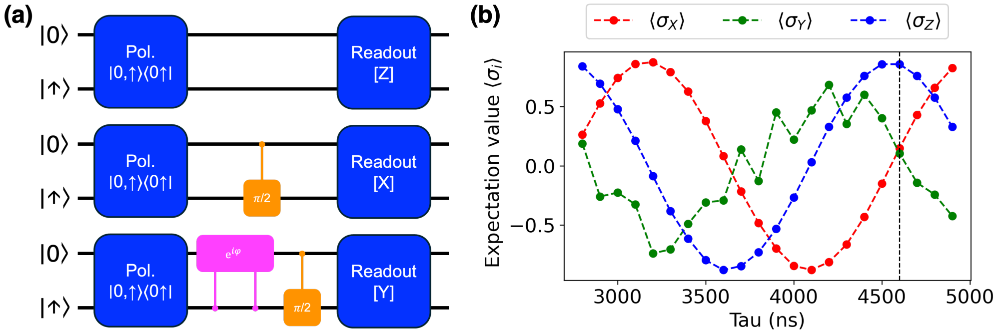

Figure S7: Nuclear spin tomography. (a) Measurement sequence for the nuclear spin tomography. For the Z basis, no additional pulse is applied. For the X basis, a waiting time of $\pi/2$ is applied. For the Y basis, additionally a phase is aquired using a MW 2π pulse with a subsequent waiting time to achieve the 90 ° rotation. **(b)** Experimental result for the nuclear spin tomography. The determined expectation values can be seen in Table S2.

For Z and X, tomography works similarly to electron spin. The measured value is used directly for the expectation value in Z, while a $\pi/2$ pulse in the x-direction is used for the expectation value in X. In this case, the $\pi/2$ pulse corresponds exactly to one waiting time of the nuclear spin precession by $\pi/2$. For the y-direction, it is not so trivial, since the method we described cannot control the precession in Y. However, this can be remedied by using the single pulse in X-direction and additionally adding a phase of the nuclear spin. Illustratively, the nuclear spin precesses when the electron spin is in the $m_s = 0$ state. If a 2π pulse is applied, the nuclear spin acquires a phase in the state $m_s = 1$, relatively to the $m_s = 0$ state. In our case, we apply two "fast" individual π pulses with a waiting time of $\tau_{\text{wait}} \approx 10$ ns between them. This value was chosen as a shorter waiting time would not be experimentally implementable and for longer waiting times the contrast of the nuclear precession would vanish due to decoherence. The schematic representation of the measurement of the three bases is shown in Figure S7a. The experimental results are as follows: the expected values for the nuclear spin in its three bases oscillate with its precession frequency. For the tomography, the value at which the desired tomography state has a maximum Z value and minimal X and Y values is taken. In this example, this is the case at $\tau = 4600$ ns and is plotted in Figure S7b.

The exact values for the tomography are shown in Table S2. Using these values, as for the electron spin, the density matrix can be reconstructed and the fidelity determined, as already shown in the main section.

Table S2: Nuclear spin tomography. Experimentally determined expectation values for the nuclear spin.

I_i	$\langle I_i \rangle$
Z	0.8574
X	0.1475
Y	0.1050

C. Two-qubit tomography

For the two-qubit tomography, the following change in the density matrix results compared to the one-qubit tomography

$$\rho = \frac{1}{4}\left(I \otimes I + \sum_{i,j} \langle S_i I_j \rangle S_i \otimes I_j\right) \tag{30}$$

and the following Bell state, which should be created.

$$|\Psi\rangle = \frac{1}{2}\begin{pmatrix} 1 & 0 & 0 & 1 \\ 0 & 0 & 0 & 0 \\ 0 & 0 & 0 & 0 \\ 1 & 0 & 0 & 1 \end{pmatrix} \tag{31}$$

The entangled state is achieved, as shown in Figure 5c in the main part, by a global π pulse on the electron spin and half a Larmor precession. Global here means that the pulse is on both ODMR transitions, i.e. both spin up and spin down for the nuclear spin. For tomography, in contrast to the one-qubit case, not 3, but 9 measurements are required to measure all bases. This is achieved by combining the 3 bases for the nuclear spin with the three for the electron spin from Figures S6a and S7b. The nuclear spin is then projected onto the electron spin for readout. In this case, timing is extremely critical, especially since the microwave pulses are sometimes very short (30 ns for the Y rotation of the nuclear spin). This ensured that, for example, the waiting time for a nuclear spin precession was from the center of the microwave pulse to the center of the next pulse in order to achieve an exact rotation.

In addition, unlike the other measurements, a time-dependent measurement where one waiting time or pulse length is swept is not possible, as otherwise the state cannot be maintained and a mixed state would settle. Therefore, each measurement was performed with a fixed time and the expected value was determined using reference measurements. For the measurements, two reference measurements were taken, one with minimum and one with maximum contrast, to which all subsequent measurements were normalized.

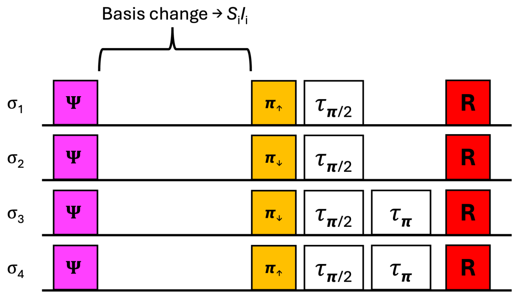

Figure S8: Tomography readout. Schematic representation of all four different readout possibilities to measure the expectation value needed for the two qubit tomography. The fourth readout was not performed due to the constraint that the sum of all σ_{i_i} equals to one.

For readout, the system was then brought into one of the two electronic states, $m_s = 0$ or $m_s = 1$, using pulse combinations. This is shown schematically in Figure S8. With these three measurements, the coefficients σ_{i_1}, σ_{i_2}, and σ_{i_3} can be determined, which are necessary for calculating the expectation values. The required fourth value can be determined using the relation $\sum_i \sigma_{i_1} = 2$. The 2 arises from the fact that, ideally, two measurements show maximum contrast, i.e., $\sigma_{i_i} = 1$, while two have minimum contrast, i.e., $\sigma_{i_i} = 0$, and thus the sum of these is 2. By halving the values, this can be normalized to 1 and using the relation $\langle\sigma_i\rangle = \sigma_{i_1} - \sigma_{i_2} - \sigma_{i_3} + \sigma_{i_4}$ the expectation value can be determined.

Table S3: Two-qubit tomography. Experimental results for the two-qubit tomography with all three experimentally determined parameters σ_{i_i} used for calculating the expectation value $\langle S_i I_j\rangle$ for each basis.

S_i	I_j	σ_{ij_1}	σ_{ij_2}	σ_{ij_3}	$\langle S_i I_j\rangle$
Z	Z	0.982	0.018	0.058	0.924
X	X	0.891	0.140	0.009	0.851
Y	Y	-0.060	0.931	0.852	-0.783
X	Y	0.433	0.385	0.471	0.144
X	Z	0.347	0.496	0.541	-0.037
Y	X	0.392	0.487	0.477	0.036
Y	Z	0.486	0.526	0.473	0.001
Z	X	0.434	0.495	0.567	-0.062
Z	Y	0.551	0.460	0.443	0.097

The results of the measurements are shown in Table S3.

Analogous to the other two tomographies of the one qubit systems, the density matrix is reconstructed using the expected values and compared with the ideal Bell state, which was already described in the main text.

---

[1] J.-Y. Zhou, Q. Li, Z.-H. Hao, W.-X. Lin, Z.-X. He, R.-J. Liang, L. Guo, H. Li, L. You, J.-S. Tang, J.-S. Xu, C.-F. Li, and G.-C. Guo, Plasmonic-Enhanced Bright Single Spin Defects in Silicon Carbide Membranes, Nano Letters **23**, 4334 (2023).

[2] C. Kurtsiefer, S. Mayer, P. Zarda, and H. Weinfurter, Stable Solid-State Source of Single Photons, Physical Review Letters **85**, 290 (2000).

[3] L. I. Childress, *Coherent manipulation of single quantum systems in the solid state*, Ph.D. thesis, Harvard University, Cambridge (2007).

[4] M. V. G. Dutt, L. Childress, L. Jiang, E. Togan, J. Maze, F. Jelezko, A. S. Zibrov, P. R. Hemmer, and M. D. Lukin, Quantum Register Based on Individual Electronic and Nuclear Spin Qubits in Diamond, Science **316**, 1312 (2007).

[5] G. Balasubramanian, I. Y. Chan, R. Kolesov, M. Al-Hmoud, J. Tisler, C. Shin, C. Kim, A. Wojcik, P. R. Hemmer, A. Krueger, T. Hanke, A. Leitenstorfer, R. Bratschitsch, F. Jelezko, and J. Wrachtrup, Nanoscale imaging magnetometry with diamond spins under ambient conditions, Nature **455**, 648 (2008).